Ocean Engineering 339 (2025) 122175

Contents lists available at ScienceDirect

Ocean Engineering

journal homepage: www.elsevier.com/locate/oceaneng

Research paper

An experimental study on the hydrodynamic performance of modular rope mesh floating solar platforms

Chenhao Mi [a,*], Patrick G. Verdin [a], Aditya Nair [a], Xiangcheng Lyu [a], Yifeng Yang [b,*], Ahmed Sherif [c], Danilo Silva [c], Luofeng Huang [a]

[a] Faculty of Engineering and Applied Sciences, Cranfield University, Cranfield, MK43 0AL, United Kingdom
[b] Department of Mechanical Engineering, University College London, London, WC1E 7JE, United Kingdom
[c] HelioRec, 1 Rue Mondésir, Nantes, 44000, France

ARTICLE INFO

Keywords:
Floating photovoltaic (FPV)
Modular design
Wave-Structure interactions
Hydrodynamic response
Mooring force
Experiments

ABSTRACT

The growing demand for sustainable energy solutions and the limitations of land-based solar installations have spurred interest in floating photovoltaic (FPV) systems. This study presents an experimental investigation of the hydrodynamic performance of modular FPV systems using an innovative Rope Mesh model. The research assesses key parameters such as the Response Amplitude Operator (RAO) and mooring forces under different wave conditions. Experiments conducted at Cranfield University evaluated the hydrodynamic responses and mooring performance of scaled-down models in controlled wave environments. The study examined the pitch and heave motion of single-body and multi-body FPV systems subjected to different wave heights and wavelengths. Results demonstrate that the modular design of the platforms can effectively withstand a range of marine conditions with minimal impact on solar panel performance in most cases. The findings provide critical insights into optimising FPV systems for nearshore and offshore applications, supporting the development of more resilient and efficient renewable energy solutions.

1. Introduction

The ongoing global energy crisis and increasing concerns about climate change have driven an urgent need for sustainable energy solutions (Owusu and Asumadu-Sarkodie, 2016). This crisis, caused by over-reliance on conventional fossil fuels, has increasingly attracted the attention of governments worldwide (Blaschke et al., 2013; Kabir et al., 2018). Renewable energy technologies, particularly solar power, have emerged as critical contenders in addressing this crisis (Breyer et al., 2022). However, the challenges of land scarcity and rising competition for space have prompted researchers to explore alternative methods for deploying solar power systems (Hernandez et al., 2015; Cazzaniga et al., 2018). As global urbanisation increases, the demand for more innovative solar deployment strategies has risen. Floating Photovoltaic (FPV) technology represents a promising solution to these challenges, offering the potential to harness solar energy on bodies of water, such as reservoirs, lakes, and oceans, without encroaching on valuable terrestrial ecosystems (Cazzaniga et al., 2018; Ranjbaran et al., 2019). In addition to this, FPV systems can benefit from the cooling effect of water, enhancing the efficiency of solar panels (Gorjian et al., 2021; Kumar et al., 2021).

The development of FPV platforms can be categorised into three main types based on their deployment environments: inshore, nearshore, and offshore (Sahu et al., 2016; Claus and López, 2022; Benjamins et al., 2024). Each environment presents unique engineering challenges, particularly regarding hydrodynamic loads and structural stability (Iglesias and Carballo, 2010; Yan et al., 2023; Djalab et al., 2024). Moving from inshore to offshore environments, factors such as wave height, wind speed, and current intensity become more unpredictable and impose more significant mechanical stresses on the platforms. While inshore FPV systems have matured commercially, the nearshore and offshore variants remain in the experimental and developmental phases due to the unpredictable marine conditions they must endure (Claus and López, 2022; Lim et al., 2024). Wind, waves, and currents impose considerable environmental stresses on offshore platforms, making them vulnerable to mechanical damage if not designed to withstand these forces (Magkouris et al., 2023; Benjamins et al., 2024). Understanding how to mitigate these environmental stresses is critical to the future development of offshore FPV systems.

In the field of offshore and nearshore FPV systems, understanding hydrodynamic behaviour is crucial for ensuring platform stability and

* Corresponding authors.
E-mail addresses: chenhao.mi.960@cranfield.ac.uk (C. Mi), yifeng.yang.19@ucl.ac.uk (Y. Yang).

https://doi.org/10.1016/j.oceaneng.2025.122175
Received 12 March 2025; Received in revised form 14 June 2025; Accepted 9 July 2025

operational efficiency. Lee et al. (2022) conducted combined experimental and numerical studies on floating solar farms under regular wave conditions, reporting motion responses and load characteristics under wave excitation. Delacroix et al. (2023) experimentally evaluated the Response Amplitude Operator (RAO) of FPV arrays, showing how platform pitch and heave are strongly affected by wave conditions. Huang et al. (2024) further demonstrated that dynamic motions can impact energy output and structural safety, especially under large wave heights.

Complementary to physical testing, recent numerical works have explored design optimisation under various marine conditions. Tang et al. (2024) developed a dynamic analysis model for multi-module FPV platforms with composite mooring, accounting for tidal variation and platform configurations. Yan et al. (2023) performed full-scale numerical simulations of multi-connected FPV systems under combined wind and wave loads, highlighting the structural responses to real-sea states.

Yang et al. (2024) conducted a comparative experimental study of FPV systems with and without breakwaters in a wave tank. While their work provided important insights into FPV hydrodynamics, the present study adopts a near-zero-impact test system that helps to minimise potential disturbances from sensor self-weight and support structures, thereby allowing clearer observation of natural platform responses.

Comparing to above FPV systems, this study presents a preliminary physical evaluation of a modular Rope Mesh floating platform concept, which integrates elastic deformation and wave-induced flexibility within a unified structure. Scaled-down experiments conducted in the Cranfield University wave tank focus on the platform's hydrodynamic behaviour under regular waves. In addition to assessing overall motion, the setup captures mooring force characteristics and local interactions between incident waves and the mounted solar panels, including dynamic coupling and panel responses. These findings provide initial insights into the motion and interaction mechanisms of flexible FPV systems, offering valuable guidance for future design and modelling developments.

Fig. 1 shows the concept of applying the Rope Mesh model to the ocean surface. Additionally, the study incorporates a near-zero-impact experimental system to assess key parameters such as RAOs and mooring forces under regular wave conditions. This design of experiment minimises interference between the testing setup and the hydrodynamic behaviour of the model. This approach ensures high precision in capturing the platform's responses, making the findings more reliable.

The geometry and manufacture of the Rope Mesh platform are detailed in Sections 2.1 and 2.2, followed by the experimental design and methodology discussed in 3. The experimental setup incorporates various mechanical resources (Section 3.1), testing configurations (Section 3.2), and parameters across multiple test cases (Section 3.3). An extensive array of sensors was used to measure critical hydrodynamic parameters to ensure the structural and operational integrity of the prototype. These sensors collect vital variables such as pitch angle, heave motion, and the tension in the mooring system, which are further analysed through RAOs and wave-panel interaction (Section 4.1). Results from the single-body model and the 2×2 multiple-body model are presented alongside mooring force analysis (Sections 4.2–4.4), followed by a discussion of how wave-panel contact impacts the outcomes (Section 4.5). The single-body and 2×2 multi-body configurations differ in total footprint due to their structural layouts, and the comparison reflects the hydrodynamic response of the respective systems under their scaled-down sizes. This study proposes a modular floating platform incorporating a rope-mesh connection scheme, aiming to improve structural flexibility and wave adaptability.

Several modular FPV projects have been recently developed to meet site-specific conditions. The Johor Strait platform in Singapore employs a compliant HDPE-based design adapted for mild wave environments, focusing on deployment efficiency and structural reliability (Zhang et al., 2024). China's Dongying project utilizes fixed-pile foundations to support rigid PV arrays in shallow offshore waters, enabling large-scale stability through rigid anchoring (Huang et al., 2023). OceanSun's Norwegian platform applies a circular tensioned membrane that directly interacts with the sea surface, promoting passive cooling and wave compliance (Huang et al., 2023).

In comparison, the key innovation of the modular Rope Mesh platform is the internal connection of components using polyamide ropes, which provide enhanced flexibility to adapt to wave motions. This directional flexibility helps relieve wave-induced forces from multiple directions and reduce long-term structural fatigue. Unlike pile-based systems, the floating design reduces construction time and cost, while allowing greater adaptability to variable site conditions. Additionally, while inspired by flexible membrane concepts, the rope-mesh platform elevates the solar panels above the waterline, offering protection against seawater splashes and reverse flow during wave impact.

Although not designed for immediate offshore deployment, the platform is evaluated through controlled wave tank experiments to capture wave-induced motions, mooring force behavior, and panel-level

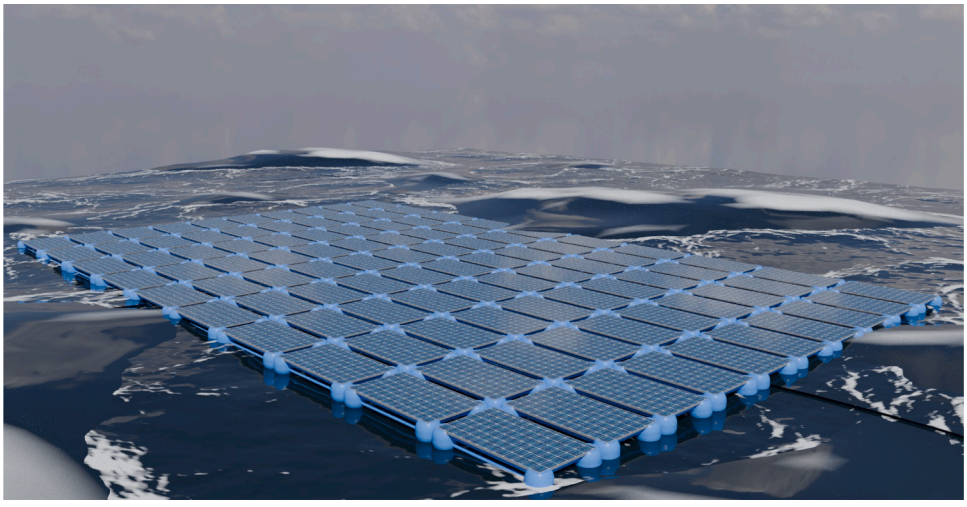

Fig. 1. Visualisation for the application of a full-scale Rope Mesh floating solar farm.

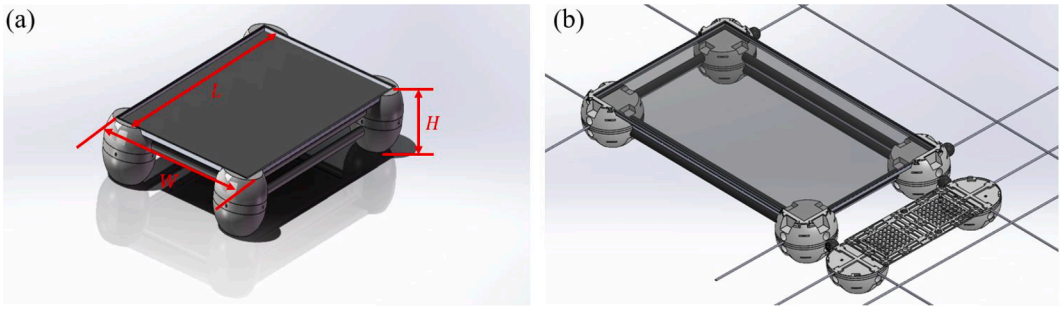

Fig. 2. Geometry of the single-body structure. (a) 3D view; (b) Perspective illustration.

interactions. These tests complement existing field-focused FPV designs and provide insight into compliant structural dynamics.

2. Geometry design of the rope mesh

2.1. Model description

The experimental design uses a modular solar floating platform developed by HelioRec Co., Ltd, based on the rope mesh structure concept. A CAD model of the single-body platform is shown in Fig. 2(a), including its main rectangular frame and four spherical floaters at each corner. Typically, the frame is used to deploy a solar cell, and four floaters provide sufficient buoyancy for the entire structure. In Fig. 2(a), L, W and H denote the length, width and heigh of the structure respectively. This structure works as the primary component of the floating system.

Fig. 2(b) provides a more comprehensive view of the testing model, illustrating the internal detailed structure and the attached footpath platform. This perspective highlights the design and configuration of the system. In particular, the major frame connected to the adjacent footpath platform by ropes. The grid-like surface of the footpath platform facilitates maintenance activities and demonstrates the flexibility of the model configuration. Such a design concept enables the floating platform easily being scaled and extended to multiple units. The rope-mesh platform consists of rigid floaters connected by polyamide ropes arranged in a square grid. This design enables compliant connections that permit local deformation under wave forcing while preserving global connectivity. The mesh structure serves to transfer and distribute loads across the platform, allowing wave energy to be absorbed along multiple paths.

2.2. Model manufacture

The scaled-down rope mesh models are designed to test their hydrodynamic performance under different wave conditions in a wave tank at Cranfield University. The scaled-down factor is 9.33. The model scale is developed through geometric scaling of the conceptual full-scale platform, ensuring proportional similarity in structural dimensions for hydrodynamic evaluation. Key geometric and physical parameters of both the model-scale and full-scale platforms are summarised in Table 1, including layout dimensions, centre of gravity, mass, and rope stiffness. Since the construction methods and materials of the scaled-down model and the full-scale model are different, the mass and rope stiffness of the full-scale model in Table 1 are mainly based on calculations and may be slightly different in actual application.

The scaled-down models, which are manufactured by the materials of ABS and Polyamide, consist of several components, including 3D-printed sphere floaters, footpath floaters, 1.5 mm polyamide ropes, rods, and solar panel units, as shown in Fig. 3 with their sizes given in Table 2, in which D represents the draft of the model tested in the still water tank. The applied ABS has a density of 1.03–1.14 g/mL, an elongation at break of 10–50 %, a yield strength of 2.96–48 MPa, a flexural strength of 2400 MPa, a Shore D hardness of 100, and a tensile strength of 2.96–43 MPa. The applied Polyamide has a density of 1.15 g/cm^3, an elongation at break of ≥50 %, a yield strength of 85 MPa, a tensile modulus of elasticity of 3300 MPa, and a Shore D hardness of 83. Two scales of Rope Mesh floating structures are applied to carry the solar panels, the single-body model and the 2 × 2 multiple-body model which are shown in Figs. 4 and 5 respectively.

Fig. 4 presents the single-body testing model, which has dimensions of 283 mm in length, 165 mm in width, and 42 mm in height. The size of the single-body model is outlined as in Table 2, these bodies are connected by Polyamide rods with dimension length $L_1 = 188$ mm or $L_2 = 70$ mm, depends on the positions of the rods, and the diameter of the cross section is $d = 6.75$ mm. Besides, the footpath floaters , which are 3D-printed with ABS material, provide additional buoyancy. The Acrylic sheet is integrated into the model to simulate the solar panels' load distribution and structural impacts. This single-body model consists of 4 spherical floaters, 12 footpath floaters, and a solar panel. The joints between floaters are equipped with 3 mm diameter plastic fishing balls to enhance flexibility and reduce interior pressure, allowing for relative motion between the components. The draft of each individual floating unit, as well as the overall assembled model, is maintained at 20 mm.

Fig. 5 presents the 2 × 2 multiple-body model, an expanded configuration designed to explore the effects of layer interactions on motion characteristics. This model shares the same construction materials as the single-body version, with 3D-printed ABS floaters and Polyamide rods. The 2 × 2 prototype has dimensions of 750 mm in length, 500 mm in width, and 42 mm in height, as shown in Table 2, which features 3 mm diameter plastic fishing balls at the joints. This multiple-body model

Table 1
Key parameters of the platform at model and full scale.

Item	Model value	Full-scale value
Single-body layout	390 × 280 mm	3640 × 2610 mm
2 × 2 layout	750 × 500 mm	7000 × 4660 mm
CG - single body	63 mm	0.59 m
CG - 2 × 2 structure	70 mm	0.65 m
Mass - single body	370 g	301 kg
Mass - 2 × 2 structure	1320 g	1072 kg
Rope stiffness	19.5 kN/m	182 kN/m

Table 2
Specifications of the components.

Item	Length or Diameter (mm)	Width (mm)	Height (mm)	Draft (mm)	Material
Sphere floater	48	–	42	20	ABS
Footpath floater	48	–	24	20	ABS
Rod	188 or 70	6.75	6.75	–	Polyamide
Single-body structure	390	280	42	20	ABS & Polyamide
2 × 2 multiple-body structure	750	500	42	20	ABS & Polyamide

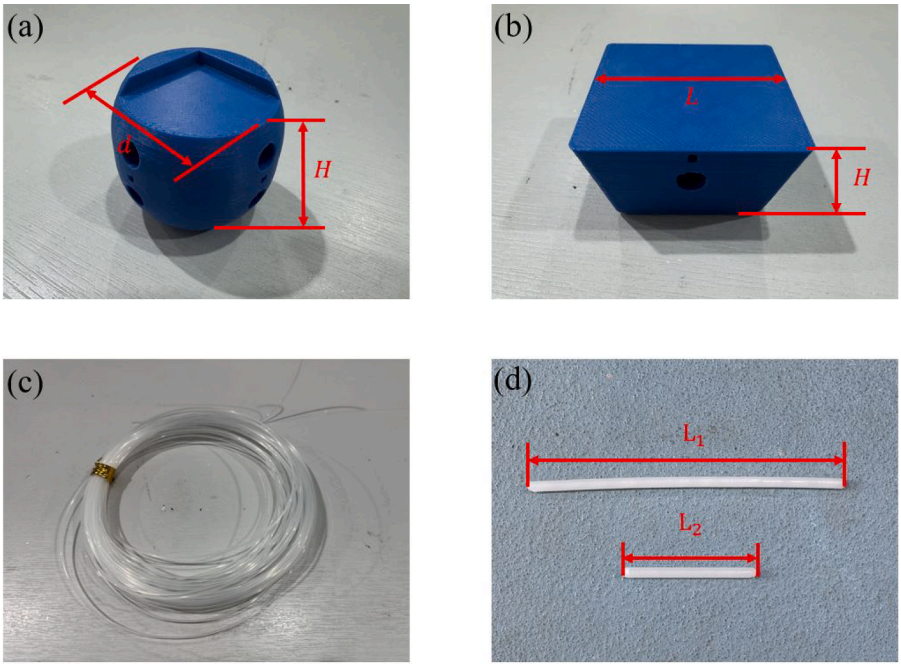

Fig. 3. Components of the rope mesh model. (a) Sphere floater; (b) Footpath floater; (c) Polyamide rope; (d) Connection rods.

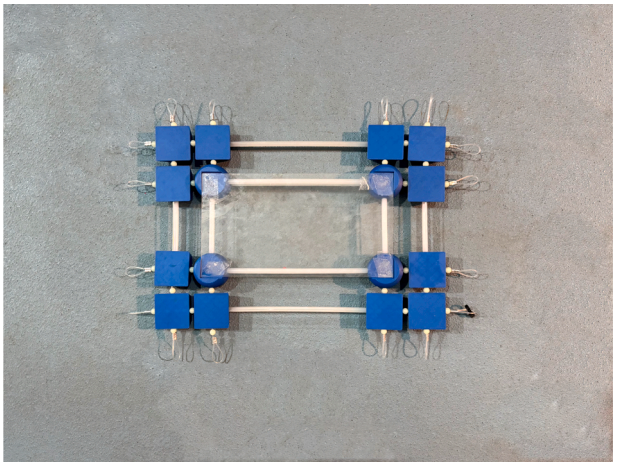

Fig. 4. Single body testing model.

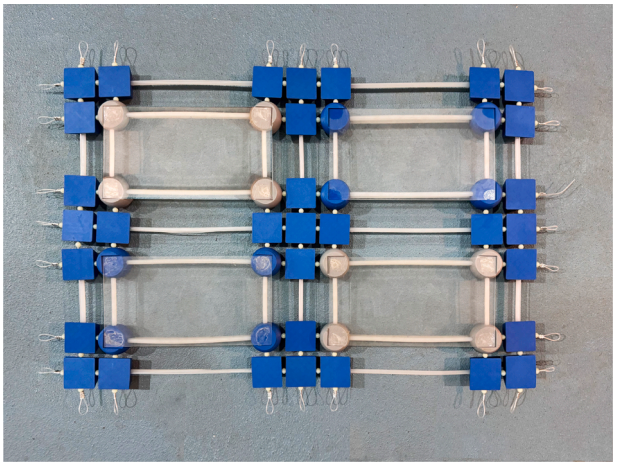

Fig. 5. 2×2 multiple body testing model.

comprises 16 spherical floats, 39 footpath floats, and 4 solar panels. The structures presented above are used for the model tests in the wave tank, particularly their interaction with water waves. The major target is to evaluate the hydrodynamic responses, including wave-induced motions (pitch & heave) and forces in mooring lines. The measured results can be reflected to that in real structure by scaling up.

3. Experimental design and methodology

3.1. Mechanical resource

The wave tank of Cranfield University is illustrated in Fig. 6, which is the same facility used by Lyu et al. (2024). The size of the tank is 30 m length, 1.5 m width and 1.5 m maximum still water depth, as also given in Table 3. The configuration of the tank is summarised as shown in Fig. 6. One end of the tank consists of three precision-controlled paddles, which can generate both regular and irregular waves. The typical maximum wave height is 280 mm, and monochromatic wave frequency ranging from 0.1 to 1.1 Hz. The other end consists of a beach type wave absorber.

3.2. Experimental setup

The sensors shown in Figs. 7 and 8 are introduced as follows:

- Load Cells (LC1, LC2): Load cells measure the tension forces in the mooring lines as the model is subjected to waves. The load cell used in the mooring system operates with a precision of 0.01 N, and both its scanning and sampling rates are set to 50 Hz to ensure adequate resolution for capturing force variations.

Table 3
Specifications of cranfield university wave tank.

Tank	Length (m)	Width (m)	Max. Depth (m)
	30	1.5	1.5
Wave generation capability	Wave Type	Max. Height	Working frequency
	Regular and irregular	280 mm peak to trough	0.1 Hz to 1.1 Hz

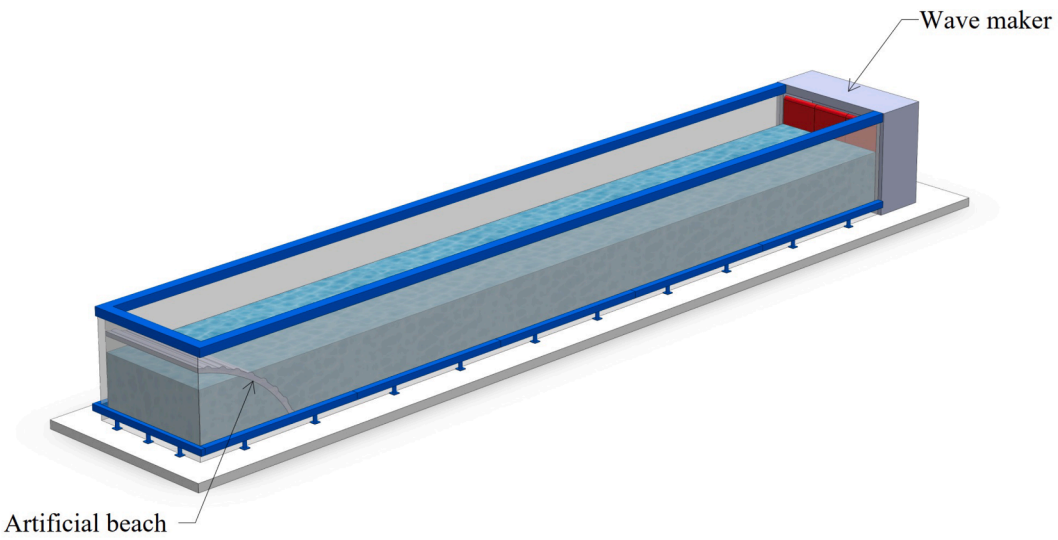

Fig. 6. 3D model of the wave tank in Cranfield University.

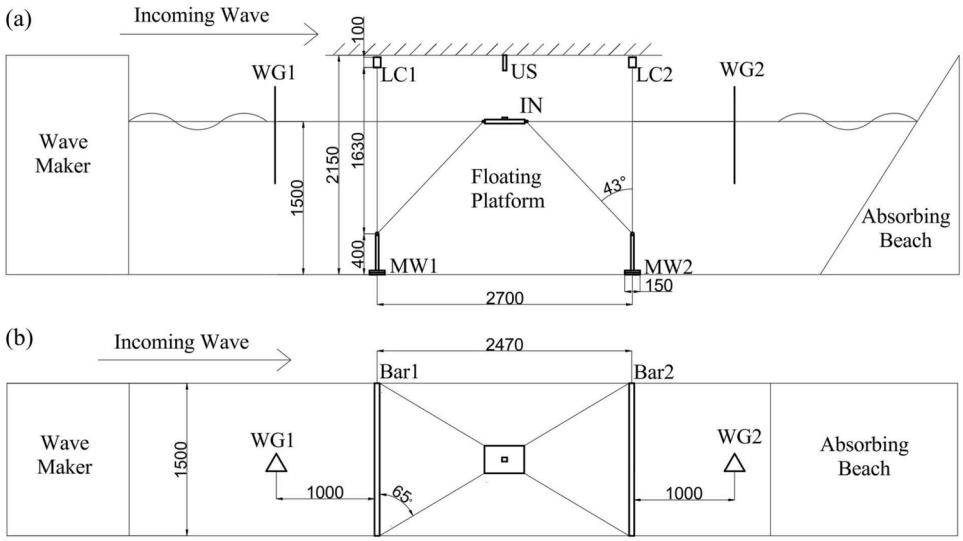

Fig. 7. The experimental setup illustration of the single-body model: (a) Profile view; (b) Top view.

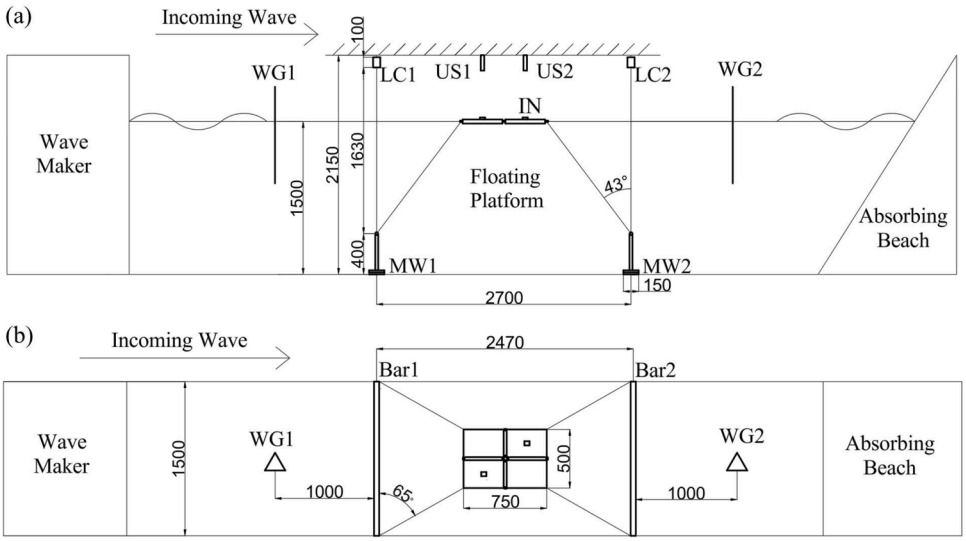

Fig. 8. The experimental setup illustration of the 2×2 multiple-body model: (a) Profile view; (b) Top view.

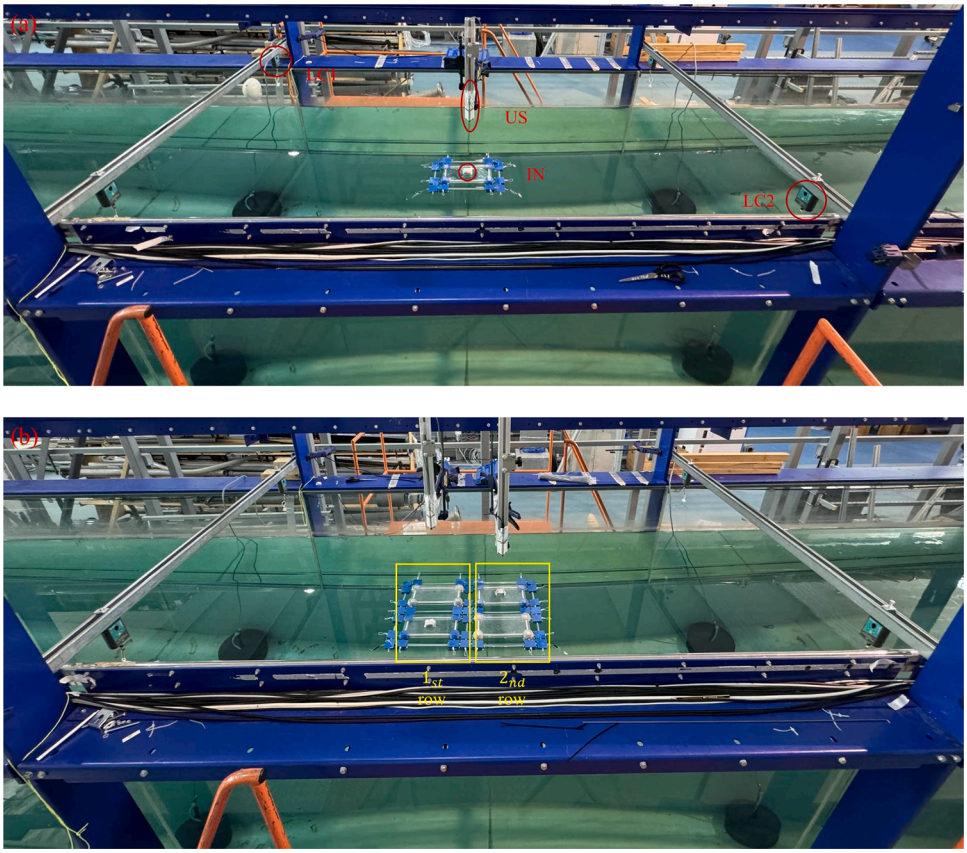

Fig. 9. Experimental setup of the testing models: (a) Single-body model; (b) 2 × 2 multiple-body model.

- Ultrasonic Sensor (US): The ultrasonic sensor measures the model's heave motion. It generates and receives ultrasonic waves to accurately track the floating platform's vertical displacement as it responds to the incoming waves.
- Inclinometer (IN): The inclinometer, attached to the centre of the solar panel, measures the model's attitude in motion. It provides detailed information on the platform's pitch angle and three-dimensional acceleration, crucial for understanding its rotational movements and overall stability under wave influence. Given the low mass of both the sensor and the panel, this placement is deemed acceptable despite a small degree of physical contact.
- Wave Gauges (WG1, WG2): The wave gauges are strategically placed upstream (WG1) and downstream (WG2) to accurately measure the wave heights generated by the wave maker. These sensors are essential for calibrating and validating the wave conditions, ensuring that the generated waves meet the desired parameters.

The experimental setups for the single-body model and the 2 × 2 multiple-body model are illustrated in Figs. 7 and 8. The illustrations present a near-zero-impact experimental system, specifically designed to minimise the influence of sensor weight on the floating platform model. The key innovation in this setup is strategically placing sensors off the platform, utilising the surrounding space in the wave tank. A pulley-like joint was introduced to redirect the mooring line vertically to a frame-mounted load cell, reducing sensor-induced interference. In the side view, the floating platform is moored by fishing lines connecting mooring weights (MW1, MW2) to Load Cells. Each mooring unit consisted of a force sensor connected in series with a spring of 30 mm in length, with a measured stiffness of 89.50 N/m, and a braided polyethylene fishing line with a diameter of 0.18 mm and a rated breaking strength of 23.7 kg. The braided polyethylene fishing line had an estimated wet weight of 7-8 mg and a tensile elastic modulus of 0.8 GPa. The fishing line is treated as a rigid link during the experiment, and the total stiffness of the mooring system was governed by the spring, resulting in a linear elastic response. A preliminary comparison experiment based on the near-zero-impact system shows that, under the spring-based mooring configuration, the system results in approximately a 10 % reduction in the load cell reading. This reduction is primarily attributed to the friction load introduced by the pulley-like joint design incorporated in the setup. Above the platform, Ultrasonic Sensors are installed to capture heave motion accurately. At the same time, Inclinometers collect the platform's pitch angles, which is essential for assessing the hydrodynamic response of the floating structure. The wave input, mooring pretension (set to 0.3 N), and sensor configuration are carefully controlled across all tests. Observed platform responses remain stable under the same wave conditions, indicating low sensitivity to minor experimental variations.

Fig. 9 illustrates the experimental setups for testing single-body and 2 × 2 multiple-body floating platforms in the wave tank of Cranfield University. In Fig. 9(a), the single-body model is positioned in the central transverse position of the wave tank. The platform is anchored by a symmetric mooring system to model the realistic engineering conditions. The mooring lines are connected to load cells, allowing for accurate measurement of mooring forces. Above the model, an ultrasonic sensor is aimed at the centre of the solar panel to record the floating platform's vertical displacement (heave motion). An inclinometer is attached to the solar panel to capture the platform's pitch angle. These sensors are strategically positioned off the platform, following the near-zero-impact design, ensuring that the sensor's weight does not interfere with the platform's natural hydrodynamic behaviour significantly. Fig. 9(b) shows the experimental setup for the 2 × 2 multiple-body model. This configuration comprises four interconnected platforms with two load cells, two ultrasonic sensors and two inclinometers. Following the setup for the single-body model, the 2 × 2 configuration uses the same sensors to

Table 4
Incident wave conditions of the single-body model.

Wave condition No.	Wave height (cm)	Wave frequency (Hz)	Wavelength/structural length (λ/L)
1	4	1	3.882
2	4	0.9	4.792
3	4	0.8	6.06
4	4	0.7	7.881
5	4	0.6	10.534
6	5	1	3.882
7	5	0.9	4.792
8	5	0.8	6.06
9	5	0.7	7.881
10	5	0.6	10.534
11	6	1	3.882
12	6	0.9	4.792
13	6	0.8	6.06
14	6	0.7	7.881
15	6	0.6	10.534
16	7	1	3.882
17	7	0.9	4.792
18	7	0.8	6.06
19	7	0.7	7.881
20	7	0.6	10.534

capture the pitch and heave motions, as well as the mooring forces. In Fig. 9(b), the 2×2 multiple-body model is divided into the 1st and 2nd rows in the experiments and subsequent analysis.

3.3. Experimental cases and parameters

The experimental cases listed in Tables 4 and 5 are designed to assess the hydrodynamic response of the single-body and the 2×2 multiple-body models. The frequency range is selected based on the capacity of the wave maker. These cases represent different combinations of wave height (H), wave frequency (f), and wavelength (λ).

The wave conditions are selected based on the scaling laws for physical model testing. The relationship between the experimental wave height (H_{exp}) and the actual wave height (H_{act}) is given by:

$$H_{exp} \times \text{Scalling ratio} = H_{act}, \tag{1}$$

which ensures that the experiments conducted at the model scale can be used to reflect the behaviour of full-scale structures. The wave height and other parameters are scaled according to this ratio to maintain physical consistency.

Table 5
Incident wave conditions of the multiple-body model.

Wave condition No.	Wave height (cm)	Wave frequency (Hz)	Wavelength/structural length (λ/L)
21	7	1.0	2.081
22	7	0.9	2.569
23	7	0.8	3.249
24	7	0.7	4.227
25	7	0.6	5.649
26	8	1.0	2.081
27	8	0.9	2.569
28	8	0.8	3.249
29	8	0.7	4.227
30	8	0.6	5.649
31	9	1.0	2.081
32	9	0.9	2.569
33	9	0.8	3.249
34	9	0.7	4.227
35	9	0.6	5.649
36	10	1.0	2.081
37	10	0.9	2.569
38	10	0.8	3.249
39	10	0.7	4.227
40	10	0.6	5.649

The wave frequency (f) and the corresponding wavelength (λ) are fundamental parameters for evaluating the hydrodynamic behaviour of floating platforms. These are calculated using the linear wave dispersion relation (Laitone, 1960):

$$\frac{2\pi}{\lambda}\tanh\left(\frac{2\pi h}{\lambda}\right) = \frac{\omega^2}{g}, \tag{2}$$

where $\omega = 2\pi f$ denotes the angular frequency, $h = 1.5$ m represents the water depth and $g = 9.81\ \text{m/s}^2$ denotes the acceleration of gravity. This relation allows for the selection of wave frequencies that are representative of various sea states.

Various periods and corresponding wave heights are selected to represent diverse wave conditions, ranging from gentle to severe. Table 4 shows incident wave heights of 4, 5, 6 and 7 cm for the single-body model, while Table 5 shows incident wave heights of 7, 8, 9 and 10 cm for the 2×2 multiple-body model. Five wave frequencies (f = 0.6, 0.7, 0.8, 0.9 and 1.0 Hz) are selected for each wave height. The wave height and frequency used in the 1:9.33 scaled model test correspond to prototype conditions of 0.37-0.93 m in wave height and 0.20-0.33 Hz. The selected wave height and frequency ranges were chosen to represent nearshore or relatively calm offshore conditions, which are commonly encountered in protected environments. These conditions serve as a controlled basis for evaluating the fundamental behaviour of the platform.

To evaluate the hydrodynamic response of the floating platform under wave-induced motions, the RAOs are introduced, which define the ratio between the motion amplitude of the platform and the amplitude of the incident waves. From Huang and Thomas (2019), this is expressed as:

$$\text{RAO}_{\text{pitch}} = \frac{a_P}{ka}. \tag{3}$$

$$\text{RAO}_{\text{heave}} = \frac{a_H}{a}. \tag{4}$$

where a_H and a_P denote the amplitude of the heave and pitch motions respectively, $a = H/2$ represents the amplitude of the wave, $k = 2\pi/\lambda$ represents the wavenumber. The non-dimensional wavelength is defined as λ/L. The time-domain response signals are transformed into the frequency domain using Fast Fourier Transform (FFT), and the dominant frequency amplitude is extracted to compute RAOs. A steady-state window of more than 10 wave cycles is selected.

4. Results and discussion

4.1. Wave interaction results

Table 6 classifies monochromatic waves interacts with a floating solar platform under various experimental conditions. Case studies are

Table 6
Wave-panel interaction levels with solar panels in experimental tests.

Case no.	Wave height (H)	λ/L				
		10.534	7.881	6.06	4.792	3.882
1 to 20	4 cm	A	A	A	A	A
	5 cm	B	B	B	B	B
	6 cm	C	C	C	C	C
	7 cm	C	C	C	C	C
Case no.	Wave height (H)	λ/L				
		5.649	4.227	3.249	2.569	2.081
21 to 40	7 cm	A	A	A	B	B
		A	A	A	A	B
	8 cm	A	A	A	B	B
		A	A	A	A	B
	9 cm	A	A	A	B	B
		A	A	A	A	B
	10 cm	A	A	A	B	B
		A	A	A	A	B

conducted for waves with different wave heights and frequencies. In the experimental cases of the 2 × 2 Multiple-body model, the results of 1st (upper) and 2nd (lower) rows are represented separately. The wave interactions are categorised into three levels, where

- Level A: Waves have no contact with the solar panels.
- Level B: Waves wash the bottom of the solar panels.
- Level C: Waves overwash the solar panels.

Table 6 shows that 17 out of 40 experimental cases across different wave heights and wavelengths fall under Level A. This suggests that the solar panels are generally well-protected from direct wave impact under most tested conditions. Under Level B conditions, where waves wash the bottom of the panels, they are concentrated in specific scenarios, particularly at smaller λ/L. This suggests that certain wave conditions, smaller wavelengths, increase wave interaction with the solar panels. The Level B conditions are more likely to occur as the wave height increases, this is particularly noticeable at the smallest λ/L, where all wave heights ($H = 5$ cm to $H = 10$ cm) are classified as Level B. Under Level C conditions, waves wash over the solar panels, meaning that the solar panels are completely exposed to the impact of the waves. These conditions generally occur under larger wave heights (typically from $H = 6$ cm and above) and mid λ/L for the single-body model. When the overwash occurs, which represents relatively revere situation for FPV system, since water may damage the electronic components.

Different level classifications will impact the practical application of FPV systems. Under Level A conditions, the solar panels experience minimal wear and tear due to the lack of significant wave impact. This will likely result in longer operational lifespans for the solar panels and lower maintenance costs. In contrast, Level B conditions imply increased exposure to waves, particularly to the bottom of the panels. This exposure can lead to higher wear and tear, potentially reducing the durability and performance of the solar panels. Increased wave contact may also lead to more frequent maintenance requirements, such as inspections, cleaning, and repairs, to ensure the panels continue to operate efficiently. Under Level C conditions, the panels are at the highest risk of damage. The impact of the waves can significantly reduce the panels' operational efficiency and durability, leading to higher long-term costs. Prolonged exposure to such conditions may result in structural damage to the platform and the need for regular inspections to ensure the system remains functional.

4.2. RAO_{Pitch} results of the testing models

Fig. 10 presents the pitch angle response in the time domain under a representative long-period wave with a wave height of $H = 7$ cm and $\lambda/L = 10.534$. The results of RAO_{Pitch} against the non-dimensional wavelength λ/L are shown in Fig. 11, including $\lambda/L = 3.882$, 4.792, 6.06, 7.881, and 10.534. This figure displays the pitch motion response for wave heights of $H = 4$, 5, 6, and 7 cm. The RAO_{Pitch} demonstrates a peak response at $\lambda/L = 6.06$ for $H = 5$ cm and $H = 7$ cm, which indicates that the structure experiences a maximum pitch motion when the wavelength is approximately six times the length of the platform. The highest values of RAO_{Pitch} are observed for $H = 7$ cm, where the RAO_{Pitch} value reaches 1.047, indicating greater rotational motion for larger waves. For $H = 6$ cm, the RAO_{Pitch} peaks at 0.988 at $\lambda/L = 4.792$, gradually decreasing as λ/L increases. For $H = 4$ cm and $H = 5$ cm, the RAO_{Pitch} reaches lower peak values of 0.851 and 0.899, respectively. This suggests that smaller waves induce less pitch motion compared to larger waves.

For these cases, the RAO_{Pitch} remains relatively constant across the range of λ/L considered, with a slight decrease as the wavelength increases beyond $\lambda/L = 7$. All wave heights show a reduction in RAO_{Pitch} as λ/L increases beyond 7, indicating that the pitch motion becomes less significant for longer wavelengths. This is particularly pronounced for $H = 4$ cm and $H = 5$ cm, where the RAO_{Pitch} drops below 0.8 for $\lambda/L > 8$. Overall, the trend suggests that, as the wave height increases, the pitch

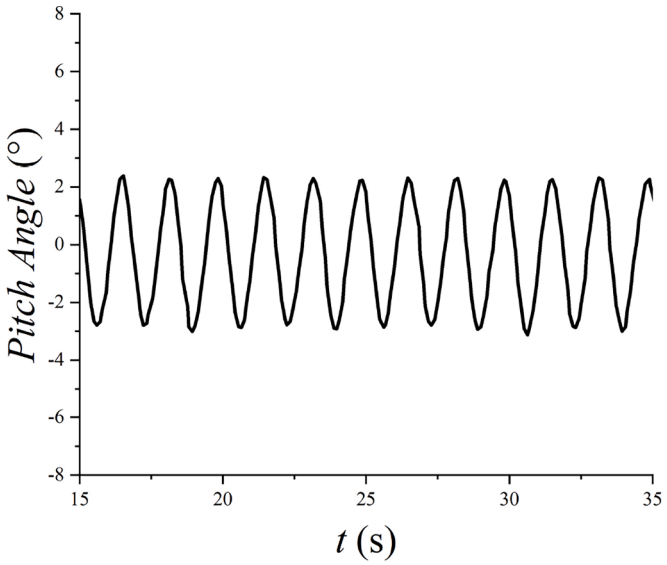

Fig. 10. Time-domain pitch angle response under the wave of $H = 4$ cm, $\lambda/L = 10.534$.

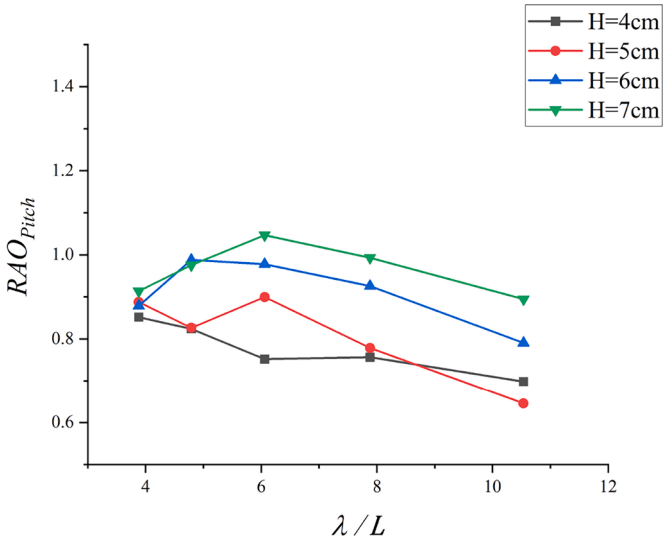

Fig. 11. RAO_{Pitch} results of the single-body model.

motion becomes more significant, particularly around $\lambda/L = 6.06$. However, for longer wavelengths, the response generally decreases across all wave heights, implying that the platform experiences less rotational motion when the wavelength highly exceeds the platform's length.

Fig. 12 shows the RAO_{Pitch} results for the 1st and 2nd rows of 2 × 2 multiple-body structure plotted against the non-dimensional wavelength λ/L, including $\lambda/L = 2.081$, 2.569, 3.249, 4.227, and 5.649. The response is presented for four wave heights: $H = 7$, 8, 9, and 10 cm. The RAO_{Pitch} of the 1st row generally increases as λ/L increases, as shown in Fig. 12(a), with the highest values observed for $H = 10$ cm at $\lambda/L = 7.881$. The maximum RAO_{Pitch} for $H = 10$ cm reaches 1.305 at $\lambda/L = 5.649$, indicating a significant pitch motion at longer wavelengths. As the wave height decreases, the maximum value of RAO_{Pitch} reduces, with $H = 7$ cm showing the smallest peak value of 1.222. For the lower wave heights, such as $H = 7$ cm and $H = 8$ cm, the response is more subdued, particularly at $\lambda/L < 3$, where By contrast, as λ/L approaches 4, the response increases steadily. The pattern suggests that larger waves induce a more pronounced pitch motion for the 1st row, particularly at longer wavelengths.

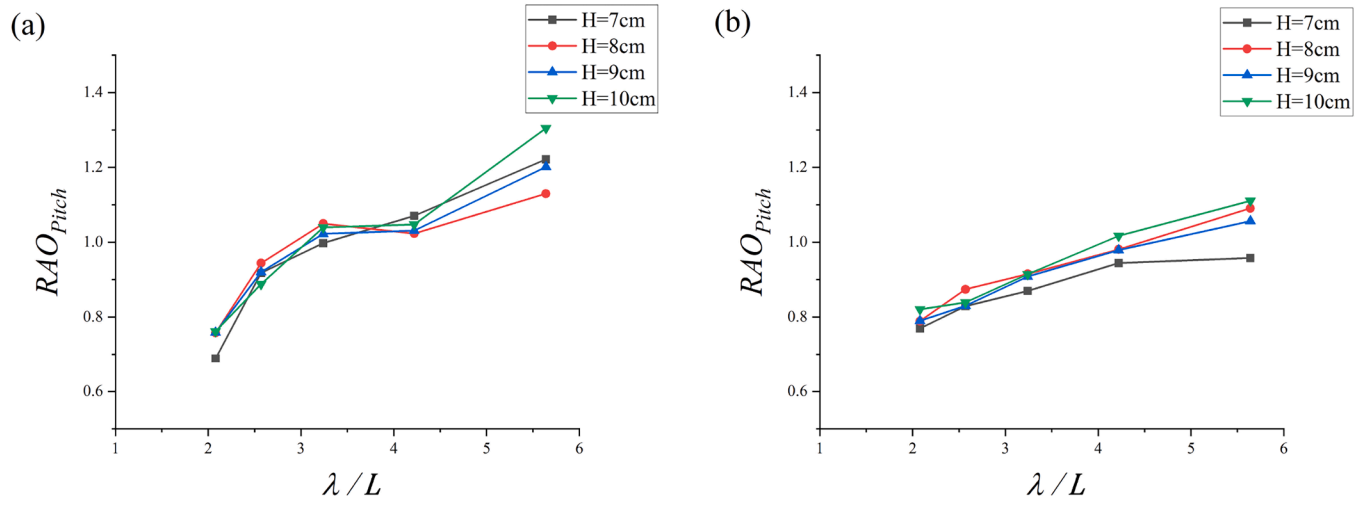

Fig. 12. RAO_{Pitch} results of the 2 × 2 multiple-body model. (a) RAO_{Pitch} results of the 1st row; (b) RAO_{Pitch} results of the 2nd row.

Fig. 12(b) presents the RAO_{Pitch} for the 2nd row of the 2 × 2 multiple-body structure under the same wave heights. In this row, the structure experiences the wave interaction after the 1st row, providing insight into how the pitch response differs for the subsequent platforms in the array. The RAO_{Pitch} for the 2nd row follows a similar upward trend with increasing λ/L, although the overall response is slightly lower compared to the 1st row. For $H = 10$ cm, the maximum RAO_{Pitch} reaches 1.111 at $\lambda/L = 5.649$, which is slightly less than the corresponding peak in the 1st row. This indicates that the 2nd row experiences reduced pitch motion, likely due to the first row's energy dissipation and wave shielding effects. For wave heights $H = 7$ cm and $H = 8$ cm, the RAO_{Pitch} remains below 1 for most values of λ/L, with a more gradual increase as λ/L enlarges. The responses for $H = 9$ cm and $H = 10$ cm show a more pronounced increase, particularly at longer wavelengths, similar to the 1st row.

The comparison between the two rows indicates that the 1st row experiences the greatest pitch motion overall, as it is directly exposed to incoming waves. In contrast, the 2nd row shows a reduction in RAO_{Pitch}, likely due to the wave energy dissipated by the 1st row. This reduction becomes less significant as the wave height increases, where the 1st row exhibits a more prominent increase in pitch motion with the increase of λ/L.

4.3. RAO_{Heave} results of the testing models

Fig. 13 presents the pitch angle response in the time domain under a representative long-period wave with a wave height of $H = 5$ cm and $\lambda/L = 6.06$. The results of RAO_{Heave} as a function of the non-dimensional wavelength λ/L are presented in Fig. 14, including $\lambda/L = 3.882$, 4.792, 6.06, 7.881, and 10.534. The figure displays the variation of RAO_{Heave} for the same wave heights $H = 4$, 5, 6, and 7 cm. RAO_{Heave} initially increases with λ/L, for all wave heights, reaching a peak around $\lambda/L = 8$. This trend indicates that, as the wavelength becomes comparable to the length of the platform, the heave response is amplified. The largest RAO_{Heave} values are observed for $H = 4$ cm, peaking at 0.93 when $\lambda/L = 7.881$, showing a greater response for smaller waves. In contrast, the smallest RAO_{Heave} values occur for $H = 7$ cm, with a maximum of 0.827. This indicates a reduction in heave motion as the wave height increases.

At $H = 5$ cm and $H = 6$ cm, the RAO_{Heave} values follow a similar pattern, with peaks at 0.900 and 0.886, respectively. As λ/L increases beyond 7, the RAO_{Heave} begins to level off, with smaller fluctuations observed, indicating a reduced structure sensitivity to longer wavelengths. The differences between RAO_{Heave} values for varying wave heights suggest that the structure experiences less pronounced vertical motion as wave height increases. The reasons include the intervention of

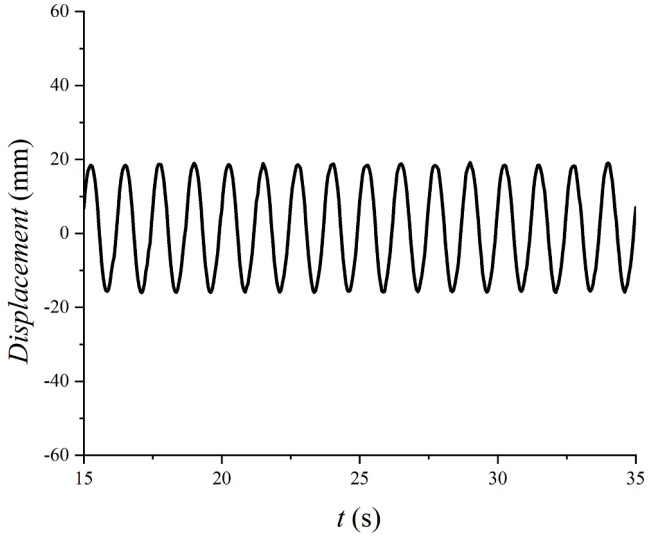

Fig. 13. Time-domain heave response under the wave of $H = 5$ cm, $\lambda/L = 6.06$.

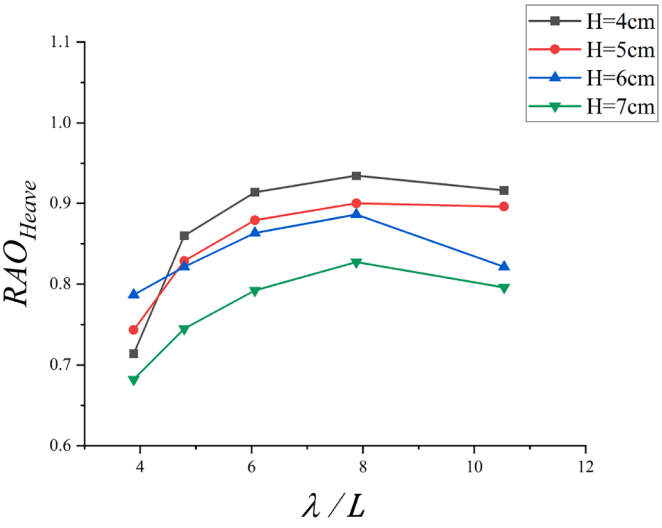

Fig. 14. RAO_{Heave} results of the single-body model.

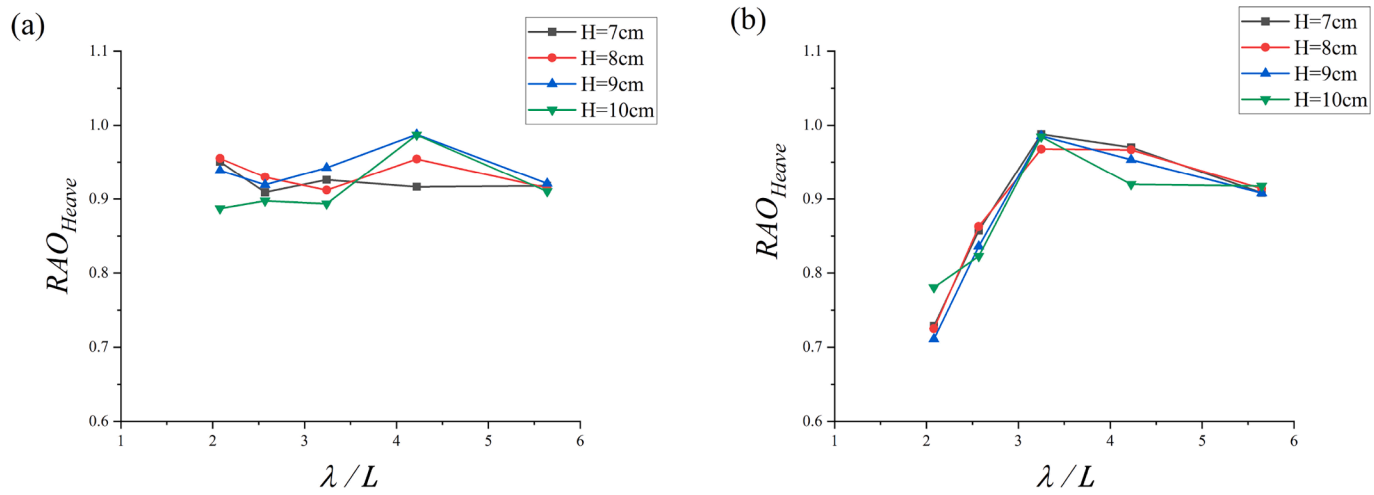

Fig. 15. RAO_{Heave} results of the 2 × 2 multiple-body model. (a) RAO_{Heave} results of the 1st row; (b) RAO_{Heave} results of the 2nd row.

mooring lines that restrict the vertical movement of the single-body structure. This is consistent with expectations, as larger waves exert greater force, but the structure's response becomes less dynamic, particularly in the heave direction. The slight reductions in RAO_{Heave} for higher wave heights, such as $H = 6$ cm and $H = 7$ cm, support this observation.

Fig. 15 illustrates the RAO_{Heave} for the 1st and 2nd rows of the 2 × 2 multiple-body structure, plotted against the non-dimensional wavelength λ/L, including $\lambda/L = 2.081$, 2.569, 3.249, 4.227, and 5.649. The RAO_{Heave} values are shown for wave heights of $H = 7$, 8, 9, and 10 cm. The 1st row RAO_{Heave} remains relatively steady across the range of λ/L values in Fig. 15(a), with values fluctuating around 0.9 to 1 for all wave heights. The response is fairly uniform, with only minor differences between the various wave heights considered, particularly for $\lambda/L < 4$. The highest peak is observed for $H = 9$ cm, reaching approximately 0.988 at $\lambda/L = 4.227$. This trend suggests that the heave motion of the 1st row is relatively insensitive to wave height, with the minimal variation in RAO_{Heave} across different conditions. The stable RAO_{Heave} values across the spectrum indicate that the 1st row experiences consistent vertical motion, regardless of the wavelength or wave height.

Fig. 15(b) shows the RAO_{Heave} for the 2nd row of the 2 × 2 multiple-body structure under the same wave heights as in Fig. 15(a). Unlike the 1st row, the 2nd row shows a more pronounced response to increasing wavelength. For $H = 7$ cm and $H = 8$ cm, the RAO_{Heave} values begin around 0.7 for $\lambda/L = 2.081$, then increase sharply, reaching a peak of around 1 at 1 around $\lambda/L = 3.249$. This peak is consistent across all wave heights, including $H = 9$ cm and $H = 10$ cm. After reaching the peak at $\lambda/L = 3.249$, the RAO_{Heave} gradually decreases for all wave heights, levelling off near 0.9 as λ/L approaches 5.649. In contrast to the 1st row, the 2nd row demonstrates a more significant rise and fall in RAO_{Heave}, particularly for shorter wavelengths ($\lambda/L < 3$). This suggests that the 2nd row is more sensitive to wavelength changes, likely due to the dissipation of wave energy by the 1st row. The peak in RAO_{Heave} for the 2nd row at wavelengths around $\lambda/L = 3$ indicates that the vertical motion is amplified in this region, after which the wave energy is reduced, leading to a decline in heave response.

Comparing Fig. 15(a) and (b), the 2nd row shows greater variation tendency in RAO_{Heave}, with a noticeable peak at around $\lambda/L = 4$. In contrast, the 1st row maintains a relatively consistent RAO_{Heave} across all the wavelengths. The lower RAO_{Heave} values for the 2nd row at shorter wavelengths suggest that the 1st row is much more affected by the wave and reflected back much of the wave energy, reducing heave motion for the subsequent platforms. At longer wavelengths, the 2nd row reaches similar RAO_{Heave} values to the 1st row, indicating a more uniform response as the waves become less frequent.

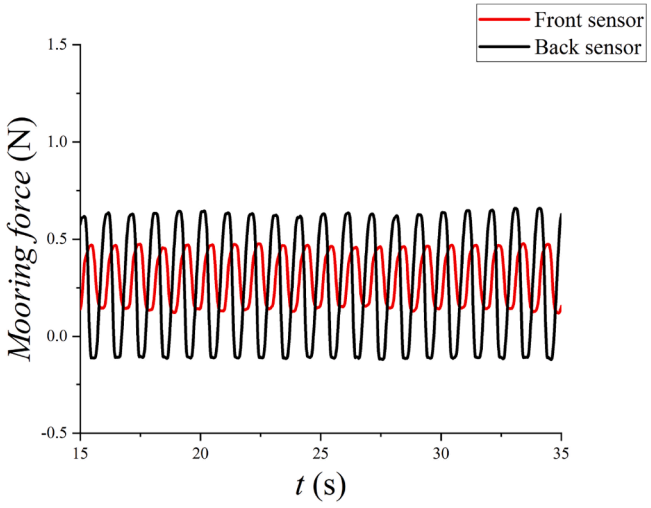

Fig. 16. Time-domain mooring force response under long-period wave (H = 4 cm, $\lambda/L = 3.882$).

4.4. Mooring force results of the testing models

Fig. 16 presents the pitch angle response in the time domain under a representative long-period wave with a wave height of $H = 4$ cm and $\lambda/L = 3.882$. Fig. 17 presents the force amplitudes on the front and the back mooring lines for the single-body model against the non-dimensional wavelength λ/L, including $\lambda/L = 3.882$, 4.792, 6.06, 7.881 and 10.534. The forces are shown for four-wave heights: $H = 4$, 5, 6, and 7 cm.

In Fig. 17(a), the front mooring force amplitudes are presented. These forces are normally smaller than those on the back mooring lines. For $H = 4$ cm, the front mooring force starts at 0.193 N and gradually increases to 0.257 N at $\lambda/L = 10.534$. For $H = 5$, 6, and 7 cm, the forces follow a similar tend, ranging between 0.20 N and 0.30 N. Across all the wave heights, the forces remain nearly constant for shorter wavelengths ($\lambda/L < 7$) but gradually increase for longer wavelengths, particularly for $H = 6$ and 7 cm.

In Fig. 17(b), the back mooring force amplitudes are presented. These forces exhibit a clear upward trend with increasing wave height.

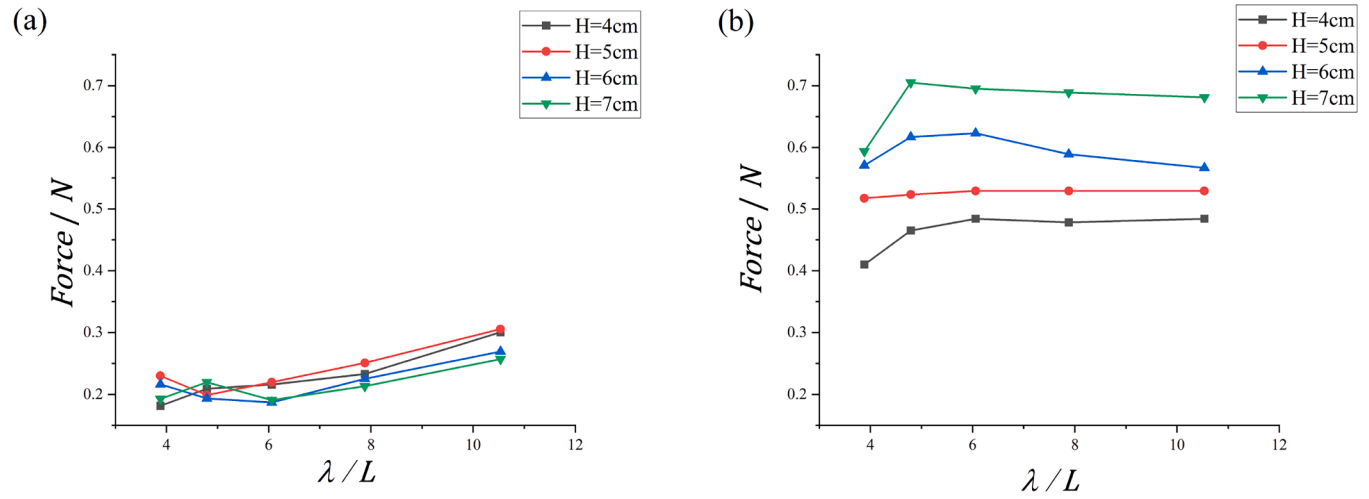

Fig. 17. Mooring force amplitude results of the single-body model. (a) Front mooring force amplitudes; (b) Back mooring force amplitudes.

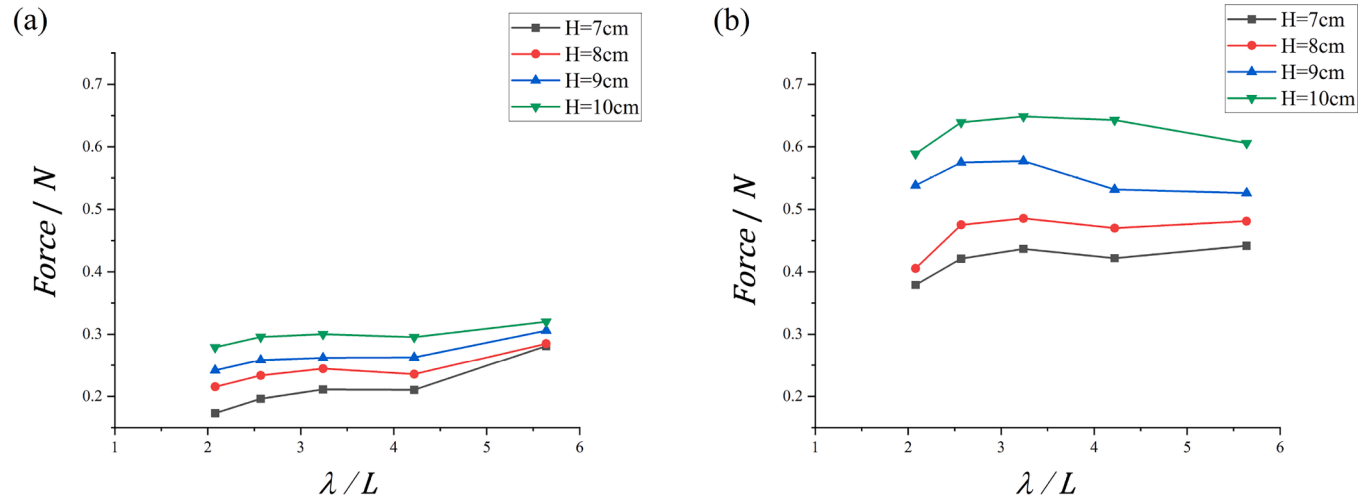

Fig. 18. Mooring force amplitude results of the 2×2 multiple-body model. (a) Front mooring force amplitudes; (b) Back mooring force amplitudes.

For $H = 4$ cm, the back mooring force starts at 0.41 N and levels off at 0.484 N. For $H = 5$ cm, the forces fluctuate around 0.52 N with minimal increasing as λ/L changes. For $H = 6$ cm, the back mooring force reaches a peak of 0.623 N at $\lambda/L = 6.06$. Finally, for $H = 7$ cm, the back mooring force starts at 0.594 N and reaches a maximum of 0.705 N at $\lambda/L = 4.792$.

Fig. 18 presents the front and the back mooring force amplitudes for the 2×2 multiple-body model plotted against the non-dimensional wavelength λ/L, including $\lambda/L = 2.081$, 2.569, 3.249, 4.227, and 5.649. The forces are presented for wave heights of $H = 7$, 8, 9, and 10 cm.

In Fig. 18(a), the front mooring force amplitudes for the 2×2 platform are shown under different wave heights. For $H = 7$ cm, the front mooring force fluctuates around 0.20 N across the range of λ/L. For $H = 8$ cm, the force is slightly higher, remaining steady at approximately 0.23 N. For $H = 9$ cm, the front mooring force increases, ranging between 0.25 N and 0.30 N. The maximum values are observed for $H = 10$ cm, starting at 0.279 N and showing only a slight increase as λ/L increases. The front mooring force shows only minor increases across all the wavelengths. These results indicate that the front of the platform experiences relatively stable forces, regardless of the wavelength.

In Fig. 18(b), the back mooring force amplitudes are presented. For $H = 7$ cm, the force is relatively low, stabilizing around 0.40 N. For $H = 8$ cm, the forces increase slightly, with values averaging around 0.45 N. For $H = 9$ cm, the back mooring line forces fluctuate between 0.50 N and 0.60 N. The highest forces are observed for $H = 10$ cm, starting at 0.589 N and peaking at 0.648 N at $\lambda/L = 3.24$. The difference in forces between wave heights is more pronounced for shorter wavelengths ($\lambda/L < 5$), while the forces stabilize across all wave heights as λ/L increases.

Through the comparison of Figs. 17 and 18, the rear mooring forces are greater than those at the front. The predominance of rear mooring forces in the Rope Mesh structure, a flexible floating system composed of polyamide ropes connecting floaters, can be attributed to several interrelated factors. Acting as both a flexible floating structure and an elastic mooring system, the hydrodynamic drift force exerts considerable influence at the rear. As wave and current interactions propagate along the structure, cumulative energy results in greater horizontal displacements, necessitating increased tension in the rear mooring elements to stabilize the system (Li et al., 2022; Kostikov et al., 2024). The Rope Mesh's flexibility enhances this effect, as the polyamide connections allow wave-induced energy to travel through the structure unevenly. This leads to non-uniform deformation, with the rear connections bearing a larger restorative load to counteract displacement (Li et al., 2022). Additionally, the spatial inhomogeneity of waves, especially in irregular or beam wave conditions, creates asymmetric forces that exacerbate the stress on the rear mooring (Li et al., 2022). The Polyamide ropes, functioning as elastic mooring lines, contribute to system dynamics. While their elasticity mitigates sharp forces during wave impacts, it also

means the rear connections must accommodate larger restoring forces under significant horizontal drift. Moreover, nonlinear coupling of wave and current forces leads to low-frequency oscillations and resonance, disproportionately affecting the rear due to its role in balancing the system's overall motion (Kostikov et al., 2024). These dynamics highlight the intricate interplay between hydrodynamic forces, structural flexibility, wave characteristics, and the unique properties of the Rope Mesh structure, establishing its rear connections as critical load-bearing components.

4.5. Discussion of the results with wave-panel contact

The solar panel was mounted in a horizontal position with minimal clearance from the water surface to allow direct assessment of wave-structure interaction within the Rope Mesh system. This configuration may increase exposure to wave impact under certain conditions. For future practical applications, panel inclination will be incorporated to simultaneously mitigate wave forces and enhance solar energy harvesting. Table 6 demonstrates that the 2×2 multiple-body structure can avoid wave overwashing even under higher wave heights and frequencies. Its flexible joints enhance the structure's ability to move with the waves, increasing wave loading capacity. The RAO results for the multiple-body structure indicate that it is less affected by wave forces, with a clear and consistent overall trend. The present 2×2 configuration primarily reflects edge-module behaviour, where mooring effects are more prominent. In larger-scale arrays, centrally located modules may exhibit different hydrodynamic characteristics dominated by adjacent-module interactions.

In contrast, in the experimental cases of single-body structure, all Level A, B and C situations occurs. These situations are related to the ratio between wave height and freeboard. Freeboard refers to the vertical distance between the deck of the floating platform and the waterline, which is a critical parameter in determining the platform's resistance to wave overwashing. In this study, the freeboard (F) of the floating platform is set to 22 mm. The ratio between the wave height (H) and the freeboard (F) can be expressed as H/F. When $H/F \geq 2.73$, corresponding to $H \geq 60$ mm, significant wave overwashing occurs. The waves exceed the platform's freeboard, directly impacting the solar panels and inducing substantial dynamic loading, rotational motion, and structural risks. The following is the discussion based on H/F.

At $H/F = 1.82$, classified as Level A, the results show minimal wave-solar panel interaction with no direct contact between the wave crest and the solar panels. As such, the RAO_{Pitch} and RAO_{Heave} values are relatively lower than those at larger wave heights, as seen in Figs. 11 and 14. In this scenario, the platform's motion is predominantly influenced by the floating structure's inherent dynamics, with minimal impact from direct wave loading on the solar panels. Additionally, the front mooring forces (Fig. 17(a)) for $H = 4$ cm remain stable and comparatively low, suggesting that the absence of wave-solar panel interaction reduces the overall load on the mooring system. The back mooring forces (Fig. 17(b)) also reflect minimal impact, as the reduced wave loading allows for more uniform force distribution along the platform.

At $H/F = 2.27$, classified as Level B, the waves wash the bottom of the solar panels, introducing partial dynamic loading on the structure. As a result, there is an observable increase in RAO_{Pitch} and RAO_{Heave} compared to $H = 4$ cm, particularly at mid-range wavelengths (λ/L between 5 and 7). This indicates that the structure begins to experience more pronounced rotational and vertical motions due to the added wave-induced forces on the solar panels. The mooring forces for $H = 5$ cm reflect this increase in dynamic loading. The front mooring force rises to approximately 0.30 N, while the front mooring force is stable at around 0.50 N (Fig. 17). This suggests that the wave-induced forces on the platform start to stabilize the system, particularly at larger wavelengths.

When $H/F \geq 2.73$, classified as Level C, the waves increase their interaction with the platform by overwashing the entire solar panel structure. This results in the highest observed values for RAO_{Pitch} and RAO_{Heave} across the tested wavelengths, as the platform undergoes substantial motion due to the direct and forceful wave impact on the solar panels. The RAO_{Pitch} (Fig. 11) shows peaks exceeding 1 for $H = 7$ cm. Similarly, the RAO_{Heave} (Fig. 14) reflects a significant increase in vertical motion for both $H = 6$ cm and $H = 7$ cm, with the most pronounced effects occurring at shorter wavelengths (λ/L between 4 and 6). This suggests that the platform's response is strongly driven by the increased hydrodynamic forces from wave overwashing, which leads to amplified rotational and heave motions. Correspondingly, the mooring forces for $H = 6$ cm and $H = 7$ cm reach their highest levels (Fig. 17), with back mooring forces peaking at approximately 0.7 N for $H = 7$ cm. This indicates that the platform's rear section is experiencing the effects of increased wave energy and subsequent force redistribution. The mooring system needs to accommodate the additional loads generated by wave overwashing, particularly at the rear layer of the structure.

The progressive increase in platform motion and mooring forces as the wave height increases from $H = 4$ cm to $H = 7$ cm highlights the impact of wave-panel contact on the system's overall performance. As the waves transition from minimal contact to overwashing the solar panels, the platform experiences a substantial increase in dynamic response, as evidenced by the RAO values for pitch and heave and the mooring forces. This wave-height sensitivity is particularly evident when the incident wave surpasses the freeboard level, leading to panel overwashing and enhanced platform flexibility. The implications of wave-panel contact on hydrodynamic response suggest that the design of FPV systems needs to account for the critical threshold where wave overwash begins to affect both platform motion and mooring load significantly. While smaller wave heights (e.g., $H = 4$ cm) can lead to amplified motions and increased structural loads, the understanding of the optimizing motion and forces on the mooring system to reduce overloading remains a design priority for FPV systems.

5. Conclusions

This study provides a detailed experimental evaluation of the hydrodynamic performance of the modular Rope Mesh floating solar platform, focusing on critical metrics such as the RAOs for pitch and heave motions, mooring force distribution, and wave-panel interactions. The results reveal that the single-body structure demonstrates higher sensitivity to wave conditions, with amplified pitch and heave responses, particularly under larger wave heights. In contrast, the 2×2 multiple-body configuration exhibits reduced wave-induced motions due to improved load sharing among interconnected modules, underscoring the advantages of modular designs in mitigating dynamic responses. The data and results presented are reported in model scale. The current study aims to assess hydrodynamic feasibility through geometry-based scaling. Due to material differences and simplifications in structural design, full-scale extrapolation is not attempted at this stage.

The near-zero-impact experimental system developed for this research played a pivotal role in ensuring accurate and reliable data collection. By minimizing the influence of sensor placement on the platform's natural hydrodynamic behaviour, this system allowed precise measurements of key parameters, such as heave motion, and mooring forces. The innovative design of the experimental setup ensured that external factors did not interfere with the structural and operational integrity of the models, thus providing robust insights into their real-world applicability.

The analysis of mooring forces further reveals a consistent pattern, where the rear mooring forces surpass those at the front across all configurations. This is primarily attributed to hydrodynamic drift forces, the flexibility of the Rope Mesh structure, and the cumulative effect of wave energy propagation along the system. These findings point out the importance of designing mooring systems capable of managing non-uniform load distributions, particularly in flexible multi-body arrangements. Wave-panel interaction analysis identifies the protective effect

of the multi-body configuration, which significantly reduces wave overwashing on downstream modules, thereby enhancing overall platform stability and durability in high-energy wave environments.

This research not only advances the understanding of the hydrodynamic behaviour of modular FPV systems but also highlights the unique contributions of the Rope Mesh design in terms of flexibility and adaptability. The integration of a near-zero-impact experimental system ensures that the findings are both precise and applicable to real-world conditions, offering a reliable foundation for further innovation.

In realistic sea states, irregular waves may intensify wave-panel interactions through mechanisms such as overwashing, impact loading, and short-period wave grouping. These effects may cause fluctuating forces on the panel surface and increase dynamic coupling between platform motion and local wave action. While not tested in this study, these interactions are expected to be more severe offshore and should be examined in future work. Future work will incorporate irregular wave tests using sea spectra to represent site-specific conditions. Additional sensors, such as water contact or pressure sensors, may be employed to quantify overwash and impact loads. Numerical simulations will also be used to extend the analysis beyond physical model limitations.

CRediT authorship contribution statement

Chenhao Mi: Writing – original draft, Visualization, Software, Methodology, Investigation; **Patrick G. Verdin:** Writing – review & editing, Validation, Supervision, Formal analysis; **Aditya Nair:** Validation, Software; **Xiangcheng Lyu:** Writing – original draft, Visualization; **Yifeng Yang:** Writing – review & editing, Validation, Methodology; **Ahmed Sherif:** Resources, Project administration, Conceptualization; **Danilo Silva:** Project administration; **Luofeng Huang:** Writing – review & editing, Supervision, Project administration, Funding acquisition, Conceptualization.

Data availability

All data underlying the results are available as part of the article and no additional source data are required.

Declaration of competing interest

The authors declare that they have no known competing financial interests or personal relationships that could have appeared to influence the work reported in this paper.

Acknowledgement

L.H. acknowledges grants received from Innovate UK (No. 10048187, 10079774, 10081314), the Royal Society (IEC\NSFC\ 223253, RG R2 232462), and UK Department for Transport (TRIG2023—No.30066).

References

Benjamins, S., Williamson, B., Billing, S.L., Yuan, Z., Collu, M., Fox, C., Wilson, B., 2024. Potential environmental impacts of floating solar photovoltaic systems. Renew. Sustain. Energy Rev. 199, 114463.

Blaschke, T., Biberacher, M., Gadocha, S., Schardinger, I., 2013. 'Energy landscapes': meeting energy demands and human aspirations. Biomass Bioenergy 55, 3–16.

Breyer, C., Khalili, S., Bogdanov, D., Ram, M., Oyewo, A.S., Aghahosseini, A., Sovacool, B.K., 2022. On the history and future of 100% renewable energy systems research. IEEE Access 10, 78176–78218.

Cazzaniga, R., Cicu, M., Rosa-Clot, M., Rosa-Clot, P., Tina, G.M., Ventura, C., 2018. Floating photovoltaic plants: performance analysis and design solutions. Renew. Sustain. Energy Rev. 81, 1730–1741.

Claus, R., López, M., 2022. Key issues in the design of floating photovoltaic structures for the marine environment. Renew. Sustain. Energy Rev. 164, 112502.

Delacroix, S., Bourdier, S., Soulard, T., Elzaabalawy, H., Vasilenko, P., 2023. Experimental modelling of a floating solar power plant array under wave forcing. Energies 16 (13), 5198.

Djalab, A., Djalab, Z., El Hammoumi, A., TINA, G.M., Motahhir, S., Laouid, A.A., 2024. A comprehensive review of floating photovoltaic systems: tech advances, marine environmental influences on offshore PV systems, and economic feasibility analysis. Sol. Energy 277, 112711.

Gorjian, S., Sharon, H., Ebadi, H., Kant, K., Scavo, F.B., Tina, G.M., 2021. Recent technical advancements, economics and environmental impacts of floating photovoltaic solar energy conversion systems. J. Clean. Prod. 278, 124285.

Hernandez, R.R., Hoffacker, M.K., Murphy-Mariscal, M.L., Wu, G.C., Allen, M.F., 2015. Solar energy development impacts on land cover change and protected areas. Proc. Natl. Acad. Sci. 112 (44), 13579–13584.

Huang, G., Tang, Y., Chen, X., Chen, M., Jiang, Y., 2023. A comprehensive review of floating solar plants and potentials for offshore applications. J. Mar. Sci. Eng. 11 (11), 2064. https://doi.org/10.3390/jmse11112064

Huang, L., Thomas, G., 2019. Simulation of wave interaction with a circular ice floe. J. Offshore Mech. Arct. Eng. 141 (4), 041302.

Huang, L., Yang, Y., Khojasteh, D., Ou, B., Luo, Z., 2024. Floating solar power loss due to motions induced by ocean waves: an experimental study. Ocean Eng. 312, 118988.

Iglesias, G., Carballo, R., 2010. Offshore and inshore wave energy assessment: Asturias (n Spain). Energy 35 (5), 1964–1972.

Kabir, E., Kumar, P., Kumar, S., Adelodun, A.A., Kim, K.H., 2018. Solar energy: potential and future prospects. Renew. Sustain. Energy Rev. 82, 894–900.

Kostikov, V.K., Hayatdavoodi, M., Ertekin, R.C., 2024. Moored elastic sheets under the action of nonlinear waves and current. Mar. Struct. 93, 103542.

Kumar, M., Niyaz, H.M., Gupta, R., 2021. Challenges and opportunities towards the development of floating photovoltaic systems. Sol. Energy Mater. Sol. Cells 233, 111408.

Laitone, E.V., 1960. Surface waves, Encycl. Phys. 3, 446–778.

Lee, J.H., Paik, K.J., Lee, S.H., Hwangbo, J., Ha, T.H., 2022. Experimental and numerical study on the characteristics of motion and load for a floating solar power farm under regular waves. J. Mar. Sci. Eng. 10 (5), 565.

Li, S., Fu, S., Zhang, S., Moan, T., 2022. Second-order hydroelastic analysis of a flexible floating structure under spatially inhomogeneous waves. Mar. struct. 86, 103306.

Lim, B.Y., Ahn, S.H., Park, M.S., Choi, J.H., Choi, H., Ahn, H.K., 2024. Prediction of fault for floating photovoltaics via mechanical stress evaluation of wind speed and wave height. IEEE Access 12, 70105–70116.

Lyu, X., Yang, Y., Mi, C., Tang, C.M., Adeboye, L., Farhan, M., Collins, S., Ou, B., Wong, A., Gordon Duffy, J., et al., 2024. A symmetric experimental study of the interaction between regular waves and a pontoon breakwater with novel fin attachments. Symmetry 16 (12), 1605.

Magkouris, A., Rusu, E., Rusu, L., Belibassakis, K., 2023. Floating solar systems with application to nearshore sites in the greek sea region. J. Mar. Sci. Eng. 11 (4), 722.

Owusu, P.A., Asumadu-Sarkodie, S., 2016. A review of renewable energy sources, sustainability issues and climate change mitigation. Cogent Eng. 3 (1), 1167990.

Ranjbaran, P., Yousefi, H., Gharehpetian, G.B., Astaraei, F.R., 2019. A review on floating photovoltaic (FPV) power generation units. Renew. Sustain. Energy Rev. 110, 332–347.

Sahu, A., Yadav, N., Sudhakar, K., 2016. Floating photovoltaic power plant: a review. Renew. Sustain. Energy Rev. 66, 815–824.

Tang, Y., Chen, X., Huang, G., Chen, M., Zhang, K., Jiang, Y., Yang, Y., 2024. Dynamic analysis of multi-module floating photovoltaic platforms with composite mooring system by considering tidal variation and platform configuration. Ocean Eng. 312, 119243.

Yan, C., Shi, W., Han, X., Li, X., Verma, A.S., 2023. Assessing the dynamic behavior of multiconnected offshore floating photovoltaic systems under combined wave-wind loads: a comprehensive numerical analysis. Sustain. Horiz. 8, 100072.

Yang, Y., Mi, C., Ou, B., Wong, A., Duffy, J.G., Wood, T., Utama, I., Chen, W., Huang, L., 2024. A comparative experimental study on the hydrodynamic performance of two floating solar structures with a breakwater in waves. Sol. Energy 284, 113029.

Zhang, C., Dai, J., Ang, K.K., Lim, H.V., 2024. Development of compliant modular floating photovoltaic farm for coastal conditions. Renew. Sustain. Energy Rev. 190, 114084.